

¹ **Estimating χ and K_T from fast-response using fast-response thermistors on**

² **traditional shipboard CTDs: sources of uncertainty and bias.**

³ Andy Pickering*

⁴ *College of Earth, Ocean, and Atmospheric Sciences, Oregon State University, Corvallis, OR.*

⁵ Jonathan Nash

⁶ *College of Earth, Ocean, and Atmospheric Sciences, Oregon State University, Corvallis, OR.*

⁷ James N Moum

⁸ *College of Earth, Ocean, and Atmospheric Sciences, Oregon State University, Corvallis, OR.*

⁹ Jennifer MacKinnon

¹⁰ *UCSD / Scripps Institute of Oceanography*

¹¹ *Corresponding author address: College of Earth, Ocean, and Atmospheric Sciences, Oregon State University, Corvallis, OR.

¹³ E-mail: apickering@coas.oregonstate.edu

ABSTRACT

14 The acquisition of turbulence data from shipboard CTD profiles is attrac-
15 tive, as it has the potential to significantly increase the amount of deep-ocean
16 mixing observations globally. While data from shear-probes are easily con-
17 taminated by motion of the instrument platform, the measurement of temper-
18 ature gradient is relatively insensitive to vehicle vibration, making it possible
19 to measure temperature gradient from a shipboard CTD rosette. The purpose
20 of this note is to investigate the error and bias in estimating the rate of dissi-
21 pation of temperature variance χ from fast thermistors mounted on traditional
22 CTD casts. The most significant source of error is associated with the fact
23 that fast-response FP07 thermistors resolve only a fraction of the temperature
24 gradient variance at the fallspeed of typical CTD casts. Assumptions must
25 be made about the wavenumber extent of the temperature gradient spectrum,
26 which scales with the rate of dissipation of turbulent kinetic energy, a quantity
27 that is not directly measured. Here we utilize observations from a microstruc-
28 ture profiler with shear probes to demonstrate the validity of our method of
29 estimating χ from thermistor data, and to assess uncertainty and bias. We then
30 apply this methodology to temperature gradient profiles obtained from χ pods
31 mounted on a CTD (the CTD- χ pod), and compare these to microstructure
32 profiles obtained almost synoptically at the equator. CTD- χ pod estimates
33 of χ compare favorably to the shear-probe microstructure measurements and
34 demonstrate that the χ pod method is not significantly biased. This supports
35 the utility of the measurement as part of the global repeat hydrography pro-
36 gram (GO-SHIP) cruises, during which this type of data has been acquired
37 during the past few years.

³⁸ **1. Introduction**

³⁹ Turbulent mixing affects the distribution of heat, salt, and nutrients throughout the global ocean.

⁴⁰ Diapycnal mixing of cold, dense water with warmer water above maintains the abyssal overturning

⁴¹ circulation (Munk 1966; Munk and Wunsch 1998), which affects global climate. Because the

⁴² turbulence that drives mixing generally occurs at scales that are not resolved in climate models,

⁴³ it must be parameterized, based on either (i) aspects of the resolved model dynamics, (ii) through

⁴⁴ higher resolution models that capture the dynamics that feed energy to turbulence, or (iii) using

⁴⁵ other parameterizations that either dynamically or statistically quantify turbulent fluxes. Recent

⁴⁶ investigations have demonstrated that these models are sensitive to the magnitude and distribution

⁴⁷ of mixing (Melet et al. 2013). A comprehensive set of measurements that spans relevant dynamical

⁴⁸ regimes is needed to constrain mixing and develop more accurate parameterizations.

⁴⁹ ~~Direct measurement of mixing~~ The most accurate measurements of turbulence are made with

⁵⁰ microstructure profilers equipped with shear probes~~is~~. Shear probes are used to measure the

⁵¹ spectra of velocity shear at small enough scales that a fit to standard inertial subrange spectral

⁵² shapes allows an estimate of the turbulent dissipation rate (ε) as a fitting parameter. This

⁵³ technique is well-suited for targeting upper-ocean processes, but can be expensive, time-intensive,

⁵⁴ and requires considerable care and expertise. Moreover, tethered profilers can't reach abyssal

⁵⁵ depths, requiring autonomous instruments to get deeper than \sim 1000-2000 m. As a result, existing

⁵⁶ measurements of diapycnal mixing, especially in the deep ocean, are sparse (Waterhouse et al.

⁵⁷ 2014). In order to obtain a larger quantity of mixing estimates, considerable work has gone

⁵⁸ into inferring mixing from measurements of the outer scales of turbulence, which are easier to

⁵⁹ obtain. One popular method is the use of Thorpe scales, where diapycnal mixing is inferred

⁶⁰ from inversions in profiles of temperature or density (Thorpe 1977; Dillon 1982). The size of

resolvable overturn is limited by the profiling speed and instrument noise (Galbraith and Kelley 1996). Several ~~While some~~ studies indicate relatively good agreement with microstructure and other observations, ~~but there are some~~ ~~there remain~~ questions about the ~~general~~ validity of the method and the assumptions made (Mater et al. 2015; Scotti 2015). Parameterizations based on profiles of shear and/or strain have also been developed and applied to estimate diapycnal mixing (Gregg 1989; Kunze et al. 2006; Polzin et al. 2013; Whalen et al. 2012, 2015) (Gregg 1989; Kunze et al. 2006). However, they rely on a series of assumptions about the cascade of energy from large to small scales (~~they assume turbulence rates are set by an energy cascade through the internal wave field~~) that are often violated; numerous studies (i.e., Waterman et al. (2013)) have shown that there is significant uncertainty associated with these parameterizations, in that there can be a consistent bias in a particular region, yet the sense of the bias (i.e., ~~overpredict over-predict~~ vs. ~~underpredict under-predict~~) is not known a priori.

~~Quanitifying Quantifying~~ turbulence from velocity shear variance (to compute the dissipation rate of turbulent kinetic energy ϵ) is challenging on moorings or profiling platforms because there is usually too much vibration and/or package motion for shear-probes to be useful. ~~Pitot-static tubes have recently been used for this purpose, plus providing independent measurements of speed (Moum 2015)~~. Other methods (i.e., optics or acoustics) may hold some promise, but lack of scatterers often precludes this type of measurement, especially in the abyss. In addition, shear probes only provide ϵ , not the ~~mixing diapycnal diffusivity~~ of scalars, K , which is often inferred from ϵ by assuming a mixing efficiency Γ (Osborn 1980) as $K = \Gamma\epsilon/N^2$, ~~which where~~ N^2 is the buoyancy frequency. A more direct measure of turbulent mixing is obtained from the dissipation rate of temperature variance χ (Osborn and Cox 1972). This has the advantage that (i) the temperature and temperature gradient can be computed and are relatively straightforward to measure, and (ii) the estimation of mixing from χ does not require assumptions about Γ . However, the spectrum

of temperature gradient extends to very small scales, so that its spectrum is seldom fully resolved (and unlike shear variance, the wavenumber extent of the temperature gradient spectrum does not scale with its amplitude, but instead depends on ε). Assumptions about the spectral shape (Kraichnan vs. Bachelor, and the value of the “constant” q) and its wavenumber extent (governed by the Batchelor wavenumber $k_b = [\varepsilon/(vD_T^2)]^{1/4}$ (Batchelor 1959)) are thus necessary to determine χ unless measurements capture the full viscous-diffusive subrange of turbulence (i.e., down to scales $\Delta x \sim 1/k_b \sim 1\text{mm}$), a criterion seldom achieved. To resolve this, we follow Alford and Pinkel (2000) and Moum and Nash (2009) and make the assumption that $K_T = K_\rho$ to determine the dissipation rate as $\varepsilon_\chi = (N^2\chi)/(2\Gamma < dT/dz >^2)$, permitting ~~estimation of k_b~~ ^{to be estimated}.

The goal of this paper is to outline and validate the methods used to compute χ and K_T with χ -~~pods~~^{pods} mounted on CTDs (Figure 1). We do this by applying our processing methodology to profiles of temperature gradient measured by thermistors on the ‘Chameleon’ microstructure profiler, which provides a direct test of our methodology. Because Chameleon is a loosely tethered profiler equipped with shear probes (Moum et al 1995)^(Moum et al. 1995), it directly measures ε and allows us to test our assumptions. Specifically, it allows us to determine biases associated with computing χ from partially-resolved temperature ~~gradient spectra~~ alone, as compared to ~~that~~
~~when it is computed by including knowledge of the dissipation rate~~^{computation that includes ε ,} which constrains the wavenumber extent of the scalar spectra. After establishing that the method works, we then compare CTD- χ pod profiles to nearby microstructure profiles.

104 **2. Data**

105 *a. EQ14*

106 Data were collected on the R/V Oceanus in Fall 2014 during the EQ14 experiment to study
107 equatorial mixing. More than 2700 Chameleon profiles were made, along with 35 CTD- χ pod
108 profiles bracketed by Chameleon profiles in order to maintain calibrations during the cruise. Most
109 Chameleon profiles were made to a maximum depth of about 250m, with CTD casts going to
110 500m or deeper. The EQ14 experiment and results are discussed in more detail in (SJ Warner, RN
111 Holmes, EH McHugh-Hawkins, JN Moum, 2016: Buoyant gravity currents released from tropical
112 instability waves, JPO, in preparation) [and Holmes et al. \(2016\)](#).

113 **3. Methods**

114 As mentioned in the introduction, the temperature gradient spectrum is rarely fully resolved
115 down to the small scales of turbulent mixing. The fraction of the spectrum resolved depends on
116 the true spectrum (a function of χ and ε), the flowspeed past the sensor (u), and the response of
117 the thermistor. The GE/Thermometrics FP07 thermistors we use typically resolve frequencies up
118 to about $f_{max} = 10 - 15$ Hz. The maximum resolved wavenumber is then equal to $k_{max} = f_{max}/u$,
119 while the wavenumber extent of the true spectrum varies with k_b (and $\varepsilon^{1/4}$). At the typical vertical
120 fall rate of a CTD rosette (~ 1 m/s), only about 20% of k_b is resolved at $\varepsilon = 10^{-10} W kg^{-1}$ (Figure
121 2). While methods have been developed to fit the observed temperature gradient spectrum to
122 theoretical forms (Ruddick et al. 2000), these work only when a larger fraction of the temperature
123 gradient spectrum is resolved. For the relatively high profiling speeds typical of CTD casts, we
124 find these methods do not work well (see appendix for [more](#) details) and therefore we use the
125 following methodology, which does not have a strongly ε -dependent bias.

126 We first outline our method for estimating χ , which relies on (i) determining the instantaneous
 127 flowspeed past the sensor, (ii) identifying periods where the signals may be contam-
 128 inated by the wake of the CTD rosette, (iii) defining the relevant values of N^2 and
 129 $(dT/dz)^2$, and (iv) applying an iterative method to compute χ and K_T . We then discuss some
 130 limitations and practical considerations that arise.

131 *a. Iterative Method for estimating χ*

132 For each ~ 1 second window, χ is estimated via the following procedure as outlined in Moum
 133 and Nash (2009). For isotropic turbulence,

$$\chi_T = 6D_T \int_0^\infty \Psi_{T_x}(k) dk \quad (1)$$

134 where D_T is the thermal diffusivity and $\Psi_{T_x}(k)$ is the wavenumber spectrum of dT/dx .

135 Note that dT/dx is not actually measured; dT/dt is measured, and dT/dx is inferred from
 136 Taylor's frozen flow hypothesis:

$$\frac{dT}{dx} = \frac{1}{u} \frac{dT}{dt} \quad (2)$$

137 where u represents the flow speed past the sensor. The wavenumber extent of the spectrum
 138 depends on the Batchelor wavenumber k_b , which is related to ε :

$$k_b = [\varepsilon / (v D_T^2)]^{1/4} \quad (3)$$

139 We assume that $K_p = K_T$ and $K_p = \Gamma \varepsilon / N^2$ where the mixing efficiency Γ is assumed to be 0.2
 140 (Moum and Nash 2009). Then dissipation rate is computed as

$$\varepsilon_\chi = \frac{N^2 \chi_T}{2\Gamma \langle dT/dz \rangle^2} \quad (4)$$

141 Typical thermistors do not resolve the spectrum out to k_b , so the measured spectrum is fit to
 142 the Kraichnan form of the theoretical scalar spectrum over the range of resolved

143 wavenumbers ($k_{min} < k < k_{max}$). The variance between the measured $[\Phi_{T_x}(k)]_{obs}$ and theoretical
144 $[\Phi_{T_x}(k)]_{theory}$ spectra at these wavenumbers is assumed to be equal:

$$\int_{k_{min}}^{k_{max}} [\Phi_{T_x}(k)]_{obs} dk = \int_{k_{min}}^{k_{max}} [\Phi_{T_x}(k)]_{theory} dk \quad (5)$$

145 An iterative procedure is then used to fit and calculate χ and ε :

146 1. First we estimate χ_T based on an initial guess of $\varepsilon = 10^{-7}$ Wkg⁻¹ and compute k_b via eq. 3.

147 We set $k_{max} = k_b/2$ or to a wavenumber equivalent to $f_{max} = 7$ Hz [i.e., $k_{max} = 2\pi(f_{max})/u$],
148 whichever is smaller. In general ~~f_{max}~~ f_{max} should be the highest value which is safely below
149 the sensor's roll-off. We chose $f_{max} = 7$ Hz in this case based on inspection of the temperature
150 gradient spectra and historical measurements of these sensors (see appendix for more details).

151 2. We then use Eq. (4) to refine our estimate of ε and k_b and recompute χ_T using Eqs. (1) and
152 (5).

153 3. This sequence is repeated and converges after two or three iterations.

154 Note that this procedure is equivalent to the explicit formulation of (Alford and Pinkel 2000),
155 except we use the Kraichnan theoretical form instead of the Batchelor spectrum for $[\Phi_{T_x}(k)]_{theory}$.

156 At wavenumbers below the spectral peak, there is little distinction between the Kraichnan and
157 Batchelor spectra, so this factor does not affect the computational bias.

158 b. CTD- χ pod Data Processing

159 The We next review the basic outline for processing each CTD- χ -pod profile is as follows: pod
160 profile. The moored χ pod instrument (Moum and Nash 2009) has a pressure sensor, compass, and
161 pitot-static tube. In contrast, the CTD- χ pod requires pressure measured by the CTD and has no
162 independent speed measurement other than dp/dt from the CTD.

1. The correct time-offset for the χ -~~pod~~-pod clock is determined by aligning highpass-filtered
 dp/dt from the 24Hz CTD data to integrated vertical accelerations measured by the
 χ -~~pod~~pod. χ -~~pod~~-pod clock drift is small, typically on the order of 1 sec/week, but it is
imperative to get records aligned within < 0.5 s so that the correct $u = w = dp/dt$ value of u
is used. In the case of the CTD- χ pod we assume u is solely due to the vertical motion of the
CTD cage, i.e. $u = dp/dt$.
2. Low-order polynomial calibration coefficients are determined to convert thermistor voltages
from χ pod to ITS90 temperature (as measured by the CTD). Figure 3 shows an example of
the aligned and calibrated CTD- χ pod timeseries for one cast. Note the significant differences
in amount of variance associated with the two sensors during down and up casts. For the
upward-mounted sensor (T1), the downcast signal is largely associated with the CTD wake,
as is the upcast for the downward-mounted sensor (T2). Only the ‘clean’ portions of the cast
(e.g., the T1 upcast and the T2 downcast) are used in the χ pod calculations.
3. Depth loops are identified and flagged in the 24Hz CTD data Figure 4(Figure 4). χ -~~pod~~-pod
data during these times are discarded since the signals are likely contaminated by the wake of
the CTD. We use a vertical velocity threshold of 0.3m/s and throw out data within 2m
of the identified loops. Even for profiles that are significantly affected by ship heaving, good
segments of data are obtained over a majority of the depths after removing contaminated data,
allowing us to compute values in nearly every 10m bin.
4. Buoyancy frequency N^2 and temperature gradient dT/dz are computed from 1-m binned
CTD data, and averaged over a scale of 10m. The results are not very sensitive to the averaging
interval (see appendix for more details).

185 5. Half-overlapping 1 sec windows of data are used to estimate χ and K_T following the methods
186 described in Moum and Nash (2009), as outlined in the previous section.

187 *c. Example Spectra and Fits*

188 Examples of the observed (from FP07 thermistor on Chameleon) and fit spectra are shown in
189 Figure 5, for two windows where a low and high dissipation rate was observed. The Chameleon
190 spectra (magenta) shown is the theoretical Kraichnan spectra for the values of χ and ε estimated
191 using the shear-probe data. The χ_{pod} fit is the estimate from applying the χ_{pod} method to just the
192 thermistor data for the same window. Note that at lower ε , a larger fraction of k_b is observed and
193 the peak of the spectrum is nearly almost resolved. At higher ε , less of the spectrum is resolved and
194 the spectral peak is well above the maximum resolved wavenumber. Even so, the iterative χ_{pod}
195 method gives an accurate estimate of χ . The χ_{pod} and Chameleon fits are performed over the same
196 wavenumber range and thus match there. However, the higher-wavenumber portions of
197 the fit spectra differ since the Chameelon Chameleon fits use the observed k_b to determine the
198 wavenumber extent.

199 *d. flowspeed past the sensor*

200 The flowspeed past the thermistor is needed to convert the measured temperature derivative
201 dT/dt to a spatial gradient. For the CTD χ_{pod} , the largest contribution to the flowspeed is
202 usually the vertical velocity of the CTD package (dp/dt), which is close to 1 m/s on average,
203 so we typically neglect the horizontal component of velocity in converting from frequency to
204 wavenumber spectra. Although usually a good approximation, errors may be introduced where
205 horizontal velocities are large. Note that because it is the total instantaneous velocity magnitude
206 that represents flow past the sensor, neglecting the horizontal component of velocity (assuming

207 $u = dp/dt$) means we are always underestimating the true flowspeed past the sensor. When the
208 CTD package is equipped with LADCP, the true flowspeed can be measured. In some cases
209 (including EQ14) where the CTD was not equipped with LADCP, it would seem that the ship's
210 ADCP could be used to estimate the horizontal component of velocity. However, because the CTD
211 does not travel perfectly vertically in strong currents, this is difficult to do in practice. In a strong
212 horizontal flow, the CTD will drift with the current while descending, lowering the flow relative
213 to the sensors. On the upcasts, the CTD will be pulled against the current, increasing the flow
214 relative to the sensors. Since the CTD in EQ14 was not equipped with LADCP, we use dp/dt as
215 the flowspeed, and estimate potential errors in the appendix.

216 4. Results

217 a. Direct Test of χ_{pod} Method

218 We begin by utilizing the highly-resolved turbulence profiler data from the freely-falling
219 turbulence profiler, Chameleon (for which both ε and χ are measured) to test the assumptions in
220 our method of estimating χ . We first apply the χ_{pod} method to each Chameleon profile, using
221 only the FP07 thermistor data. These results, which we will refer to as $\chi_{\chi} \chi_{\chi}^{\text{cham}}$ and assume
222 no independent knowledge of ε , are then compared with χ_{ε} to $\chi_{\varepsilon}^{\text{cham}}$, computed by integrating
223 the theoretical temperature gradient spectrum with where k_b is computed directly from shear-
224 probe derived ε . Qualitatively, χ_{χ} and χ_{ε} $\chi_{\chi}^{\text{cham}}$ and $\chi_{\varepsilon}^{\text{cham}}$ show very similar depth and time
225 patterns (Figure 6) and appear to agree in magnitude, suggesting the method works well. A more
226 quantitative comparison is made with a 2-D histogram (Figure 7), showing shows the two are well-
227 correlated over a wide range of magnitudes five orders of magnitude. The distribution of \log_{10} of

228 the χ ratios is approximately normal, with a mean of $\mu = -0.1$ and standard deviation of $\sigma = 0.51$.
229 This indicates a low bias of χ_{χ}^{cham} relative to $\chi_{\varepsilon}^{cham}$ of 20% and random variation of a factor of 3.

230 b. *CTD χ -pod* - Chameleon Comparison

231 Having demonstrated that the method works using Chameleon data, we now compare ~~χ~~ χ_{χ}^{ctd}
232 from CTD-mounted χ pods to $\chi_{\varepsilon} \chi_{\varepsilon}^{cham}$. In contrast to the Chameleon data, the CTD is more
233 strongly coupled to the ship, and therefore subject to more vibration, heaving, and ~~artificial~~ artificial
234 turbulence created by the rosette. A total of 35 CTD- χ pod casts were performed, bracketed with
235 Chameleon profiles immediately before and after. We first compare CTD- χ pod profiles to the
236 mean of the two Chameleon profiles bracketing each cast, both averaged in 5m depth bins (Figure
237 8). The two are correlated, with considerable scatter. A histogram of the log of ratios is approxi-
238 mately normal and has a mean of -0.31 , indicating a ~~possible~~ small negative bias. Since we expect
239 significant natural variability in turbulence even between adjacent Chameleon profiles, we investi-
240 gate further to determine if the observed χ pod variability is of a similar magnitude or greater than
241 expected. Scatter plots of before vs. after Chameleon profiles (not shown), typically separated by
242 about an hour, show a similar level of scatter as the differences between methods, suggesting that
243 the observed differences (Figure 8) can be explained by natural variability in turbulence. This is
244 further demonstrated by histograms of the ratio of χ from adjacent casts (Figure 9) which show
245 that the variability between CTD χ pod and Chameleon casts is similar to the natural variability be-
246 tween before/after Chameleon profiles. Profiles from all CTD-Chameleon pairs averaged in time
247 and 40m depth bins (Figure 10) overlap within 95% confidence limits at all depths where there
248 exists good data for both. Averages of subsets of these profiles that were clustered in position/time
249 (not shown) also agree well. We conclude that the variability between CTD χ pod and Chameleon
250 profiles is indistinguishable from natural variability in turbulence levels.

251 **5. Discussion**

252 We have shown that χ can be accurately estimated from χ pods attached to CTD rosettes. The
253 method also estimates K_T and ϵ , but we have ~~not discussed it here since it involves left discussion~~
254 ~~of these for a future paper since they involve~~ more assumptions and uncertainties. One major
255 assumption is the mixing efficiency Γ . A value of 0.2 is commonly assumed, but evidence sug-
256 gests this may vary significantly. Moum and Nash (2009) found a bias ~~in χ~~ of up to 1.6 for Γ
257 values ranging from 0.1 to 0.35. Another major assumption in the χ pod method is that $K_T = K_\rho$.
258 ~~Preliminary investigation on this data suggests that this assumption does not hold here and may~~
259 ~~be responsible for a negative bias in ϵ , but more work is needed to verify this. However we have~~
260 ~~shown that even if ϵ estimates are biased, χ and K_T are still robust.~~, which should be true where
261 ~~density is dominated by temperature.~~

262 The goal of CTD- χ pods is to expand the number and spatial coverage of ocean mixing observa-
263 tions. ~~The census of Waterhouse et al. (2014) found 10 locations where full-depth microstructure~~
264 ~~profiles were taken (see their figure 1c), all of which had between 11 and 100 profiles.~~ We have
265 already deployed ~~instruments~~ ~~CTD χ pods~~ during several process experiments and on several GO-
266 SHIP repeat-hydrography cruises, ~~obtaining more than 1700 full-depth profiles of χ over a wide~~
267 ~~range of locations.~~ We plan to continue regular deployment on GO-SHIP and similar cruises,
268 adding χ ~~and K_T~~ to the suite of variables regularly measured. The expanding database of mixing
269 measurements from CTD- χ pods will also enable testing of other commonly-used or new mixing
270 parameterizations. This has the potential to be transformative for the field, allowing the commu-
271 nity to develop and test global turbulence parameterizations, use estimates of turbulence along
272 with the CLIVAR repeat hydrography data for inverse models and water mass modification cal-

273 culations, identify hotspots of turbulence to target with future process experiments, and compare
274 with in-situ chemical and biological measurements made routinely on repeat hydrography cruises.

275 **6. Conclusions**

- 276 • The χ pod method for estimating χ and K_T was directly applied to temperature gradients
277 measured by the Chameleon microstructure profiler on > 2700 profiles during the EQ14
278 cruise. The estimated χ_χ agrees well with χ_ε calculated using ε from shear probes over a
279 wide range of magnitudes (Figure 7) with little or no bias, demonstrating that the method
280 works.
- 281 • CTD- χ pod profiles were also compared to nearby Chameleon profiles during the cruise. Vari-
282 ability between CTD- χ pod and Chameleon estimates of χ is indistinguishable from natural
283 variability between Chameleon profiles. Time-averaged profiles of χ from both platforms
284 agree within 95% confidence limits, and no significant bias was detected between the esti-
285 mates of χ .
- 286 • We conclude that estimates of χ and K_T made from the CTD- χ pod platform are robust and
287 reliable.

288 *Acknowledgments.* The EQ14 experiment was funded by ??? budget (NSF?) 1256620. We
289 thank the Captain and crew of R/V Oceanus. Also thank people who helped collect the data, those
290 who Pavan Vutukur, Craig Van Appledorn, Mike Neeley-Brown made the sensors,etc... Aurelie
291 Moulin, Ryan Holmes, Sally Warner and Anna Savage helped to collect the data.

292 APPENDIX A

293 **Sensitivity Analysis**

294 **A1. Flowspeed Past Sensor**

295 To ~~quauitify~~ quantify the potential error in the CTD- χ pod calculations from ignoring horizontal
296 velocities and assuming the flow speed is equal to the vertical speed of the CTD rosette, we re-
297 peated the calculations with constant offsets added to the flowspeed. ~~Since~~ Note that since the total
298 magnitude of velocity is used, dp/dt is a minimum estimate of the true speed. Adding 0.1(1)m/s
299 results in a mean percent error of ~~14(58-14(-58))~~ percent (Figure 11), small compared the large
300 natural variability in turbulence and uncertainty in our measurements. Note that increasing the
301 velocity tends to result in smaller values of χ , since it shifts the spectrum to lower wavenumbers.

302 We also looked for any systematic biases associated with flowpseed. We found ~~the~~that χ was
303 biased high for very small speeds ($u < 25\text{cm/s}$). This could be ~~assoicited~~associated with contam-
304 ination by CTD wake or entrained water when the CTD slows. These values were discarded for
305 our analysis.

306 **A2. N^2 and dT/dz**

307 We investigated the sensitivity of the calculations to the scale over which N^2 , dT/dz are aver-
308 aged. The iterative method to estimate chi requires the background stratification N^2 and temper-
309 ature gradient dT/dz . The estimate of χ is ~~insenstive~~insensitive to these scales. However, ~~while~~
310 dissipation rate ϵ and diffusivity K_T are more strongly affected because they are linearly related
311 to these values. Computing N^2 and dT/dz over smaller scales (less than a few m) results in larger
312 values and hence some larger values of K_T .

313 APPENDIX B

314 **Test of MLE fitting method**

315 We also tested the spectrum fitting method of Ruddick et al. (2000) and compared to our χ pod
316 method. The MLE method works well and gives similar results to our method at true ε values
317 less than about 10^{-9} , but severely underestimates χ at larger values of epsilon, where only a small
318 fraction of the spectrum is resolved (Figure 12). At lower profiling speeds we would expect the
319 MLE method to work better, as more of the spectrum will be resolved for a given value of *epsilon*.

320 APPENDIX C

321 **Thermistor Frequency Response**

322 Prior to 2009, the transfer function for each FP07 thermistor was measured by profiling adjacent
323 to a thermocouple in Yaquina Bay, OR. However, measuring the transfer function for each indi-
324 vidual thermistor proved too expensive and time-consuming, and since that time a generic transfer
325 function has been used. Figure 13 shows the ~~measured~~ measured transfer functions for 2008. The
326 majority of the ~~the~~ transfer functions are similar for ~~at~~ frequencies up to about 10 Hz, and begin to
327 significantly differ above that. To estimate the potential error in not using a transfer function, we
328 calculated the % of spectral variance captured for each of the measured functions. For frequencies
329 up to 7Hz, more than 95% is captured for 88% of the measured functions. If frequencies up to
330 15hz are used, more than 95 % variance is captured only 67% of the time. Using only frequencies
331 up to 7Hz (where the transfer function is equal to or very close to unity) avoids the issue of the
332 unknown transfer functions.

333 **References**

334 Alford, M., and R. Pinkel, 2000: Patterns of turbulent and double diffusive phenomena: Observa-
335 tions from a rapid profiling conductivity probe. *J. Phys. Oceanogr.*, **30**, 833–854.

- 336 Batchelor, G. K., 1959: Small-scale variation of convected quantitites like temperature in turbulent
337 fluid. *J. Fluid Mech.*, **5**, 113–139.
- 338 Dillon, T. M., 1982: Vertical overturns: A comparison of Thorpe and Ozmidov length scales. *J.*
339 *Geophys. Res.*, **87**, 9601–9613.
- 340 Galbraith, P. S., and D. E. Kelley, 1996: Identifying overturns in CTD profiles. *J. Atmos. Ocean.*
341 *Tech.*, **13**, 688–702.
- 342 Gregg, M., 1989: Scaling turbulent dissipation in the thermocline. *J. Geophys. Res.*, **94 (C7)**,
343 9686–9698.
- 344 Holmes, R., J. Moum, and L. Thomas, 2016: Evidence for seafloor-intensified mixing by surface-
345 generated equatorial waves. *Geophysical Research Letters*, **43 (3)**, 1202–1210.
- 346 Kunze, E., E. Firing, J. Hummon, T. K. Chereskin, and A. Thurnherr, 2006: Global abyssal mixing
347 inferred from lowered ADCP shear and CTD strain profiles. *Journal of Physical Oceanography*,
348 **36 (8)**, 1553–1576.
- 349 Mater, B. D., S. K. Venayagamoorthy, L. S. Laurent, and J. N. Moum, 2015: Biases in Thorpe scale
350 estimates of turbulence dissipation Part I: Assessments from large-scale overturns in oceanographic
351 data. *J. Phys. Oceanogr.*, **45 (2015)**, 2497–2521.
- 352 Melet, A., R. Hallberg, S. Legg, and K. L. Polzin, 2013: Sensitivity of the ocean state to the
353 vertical distribution of internal-tide-driven mixing. *J. Phys. Oceanogr.*, **43 (3)**, 602–615, doi:
354 <http://dx.doi.org/10.1175/JPO-D-12-055.1>.
- 355 Moum, J., M. Gregg, R. Lien, and M. Carr, 1995: Comparison of turbulence kinetic energy dis-
356 sipation rate estimates from two ocean microstructure profilers. *Journal of Atmospheric and*
357 *Oceanic Technology*, **12 (2)**, 346–366.

- 358 Moum, J., and J. Nash, 2009: Mixing measurements on an equatorial ocean mooring. *J. Atmos.*
359 *Ocean. Tech.*, **26**, 317–336.
- 360 Moum, J. N., 2015: Ocean speed and turbulence measurements using pitot-static tubes on moor-
361 ings. *Journal of Atmospheric and Oceanic Technology*, **(2015)**.
- 362 Munk, W., and C. Wunsch, 1998: Abyssal recipes II: energetics of tidal and wind mixing. *Deep-*
363 *Sea Res. Part I*, **45**, 1977–2010.
- 364 Munk, W. H., 1966: Abyssal recipes. *Deep-Sea Res.*, **13**, 707–730.
- 365 Osborn, T. R., 1980: Estimates of the local rate of vertical diffusion from dissipation measure-
366 ments. *J. Phys. Oceanogr.*, **10**, 83–89.
- 367 Osborn, T. R., and C. S. Cox, 1972: Oceanic fine structure. *Geophys. Fluid Dyn.*, **3**, 321–345.
- 368 Polzin, K. L., A. C. Naveira Garabato, T. N. Huussen, B. M. Sloyan, and S. Waterman,
369 2014: Finescale parameterizations of turbulent dissipation. *Journal of Geophysical Research:*
370 *Oceans*, **119 (2)**, 1383–1419, doi:10.1002/2013JC008979, URL <http://dx.doi.org/10.1002/2013JC008979>.
- 371 Polzin, K. L., A. C. Naveira Garabato, T. N. Huussen, B. M. Sloyan, and S. N. Waterman, 2013:
372 Finescale parameterizations of turbulent dissipation. *Rev. Geophys.*, **submitted**.
- 373 Ruddick, B., A. Anis, and K. Thompson, 2000: Maximum likelihood spectral fitting: The Batch-
374 elor spectrum. *J. Atmos. Ocean. Tech.*, **17**, 1541–1555.
- 375 Scotti, A., 2015: Biases in Thorpe scale estimates of turbulence dissipation Part II: Energetics
376 arguments and turbulence simulations. *J. Phys. Oceanogr.*, **45 (2015)**, 2522–2543.

- 378 Thorpe, S., 1977: Turbulence and mixing in a Scottish Loch. *Philos. Trans. R. Soc. London Ser.*
379 *A*, **286**, 125–181.
- 380 Waterhouse, A. F., and Coauthors, 2014: Global patterns of diapycnal mixing from measurements
381 of the turbulent dissipation rate. *J. Phys. Oceanogr.*, **44** (7), 1854–1872.
- 382 Waterman, S., A. C. N. Garabato, and K. L. Polzin, 2013: Internal waves and turbulence in the
383 antarctic circumpolar current. *Journal of Physical Oceanography*, **43** (2), 259–282.
- 384 Whalen, C. B., J. A. MacKinnon, L. D. Talley, and A. F. Waterhouse, 2015: Estimating the
385 mean diapycnal mixing using a finescale strain parameterization. *Journal of Physical Oceanog-
386 raphy*, **45** (4), 1174–1188, doi:10.1175/JPO-D-14-0167.1, URL [http://dx.doi.org/10.1175/
387 JPO-D-14-0167.1](http://dx.doi.org/10.1175/JPO-D-14-0167.1).
- 388 Whalen, C. B., L. D. Talley, and J. A. MacKinnon, 2012: Spatial and temporal variabil-
389 ity of global ocean mixing inferred from argo profiles. *Geophys. Res. Lett.*, **39** (L18612),
390 doi:10.1029/2012GL053196.
- 391 Portion of a CTD cast showing depth vs time (top) for a portion of an upcast, with data flagged
392 as loops in red. Lower panel shows corresponding xpod timeseries of dT/dt for that time with
393 discarded loop data in red. Note that variance tends to be larger during depth loops due to entrained
394 water and CTD-induced turbulence.

395 LIST OF FIGURES

396	Fig. 1. Photo of CTD rosette during EQ14 with χ -pods-pods attached.	23
397	Fig. 2. Ratio of the maximum observed wavenumber $k_{max} = f_{max}/u$ to the Batchelor wavenumber k_b for different values of ϵ , assuming a $f_{max} = 7\text{Hz}$. Each line is for a different flowspeed.	24
399	Fig. 3. Example timeseries from one CTD cast during EQ14. a) CTD pressure. b) Fallspeed of CTD (dp/dt) .c) Vertical and horizontal accelerations measured by χ -pod-pod. d) Temperature from CTD and (calibrated) χ -pod-pod sensors. T2 is offset slightly for visualization. e) Temperature derivative dT/dt measured by the upward-looking χ -pod-pod sensor T1. f) Temperature derivative dT/dt measured by the downward-looking χ -pod-pod sensor T2.	25
404	Fig. 4. Portion of a CTD cast showing depth vs time (top) during an upcast, with data flagged as loops in red. Lower panel shows corresponding χ -pod timeseries of dT/dt for that time with discarded loop data in red. Note that variance tends to be larger during depth loops due to entrained water and CTD-induced turbulence.	26
408	Fig. 5. Example Two example temperature gradient spectra from an EQ14 Chameleon profile, for high (top) and low (bottom) values of ϵ . Solid black lines with circles show the observed temperature-gradient spectra from the thermistor on Chameleon. Dashed black line shows the fitted theoretical Kraichnan spectra for estimated by applying the χ -pod estimates method to the thermistor data only. Magenta line is Kraichnan spectra for Chameleon χ and ϵ measured at the same depth, using the shear probe data as well. Vertical dashed blue(red) lines indicate the minimum (maximum) wavenumber used in the χ -pod calculation. The Batchelor wavenumber k_b is also indicated by the vertical cyan-magenta line.	27
416	Fig. 6. Depth-time plots of $\log_{10}\chi$ from both methods for EQ14 data. Top: χ -pod method using only FP07 data from Chameleon. Black diamonds indicate casts used for comparison with CTD- χ -pod profiles. Bottom: Chameleon measurements using FP07 and shear probe data.	28
419	Fig. 7. Left: 2D histogram of $\log_{10}(\chi)$ from Chameleon (x-axis) and χ -pod method (y-axes). Values from each profile were averaged in the same 5m depth bins. Right: Normalized histogram of $\log_{10}[\chi_{\chi}/\chi_{\epsilon}] \log_{10}[\chi_{\chi}^{cham}/\chi_{\epsilon}^{cham}]$. Vertical dashed line indicates the mean of the distribution.	29
423	Fig. 8. Left: Scatter plot of χ from CTD- χ -pod profiles versus the mean of bracketing Chameleon profiles. Black dashed line shows 1:1, red are $\pm 10\chi$. Right: Normalized histogram of the log of ratios.	30
426	Fig. 9. Histogram of \log_{10} of the ratio of χ for nearby casts. The first set is for the before (eham1 $\chi_{\epsilon 1}^{cham}$) and after (eham2 $\chi_{\epsilon 2}^{cham}$) Chameleon profiles. The 2nd is CTD- χ -pod profiles (χ_{χ}^{ctd}) versus the before(eham1 $\chi_{\epsilon 1}^{cham}$) profiles. The last is CTD- χ -pod profiles (χ_{χ}^{ctd}) versus the after(eham2 $\chi_{\epsilon 2}^{cham}$) profiles. Dashed lines show the medians of each set. Note that bias is small/zero, and the variability (spread) between CTD/cham is similar to the natural variability between cham profiles.	31
432	Fig. 10. Time mean of χ for all CTD- χ -pod - Chameleon cast pairs, with 95% bootstrap confidence intervals.	32
434	Fig. 11. Histogram of % error for χ computed with constant added to fallspeed, in order to examine sensitivity to fallspeed. Vertical lines indicate the mean of each distribution.	33

Fig. 12. Left: 2D histograms of χ computed using the ~~interative~~ ~~iterative~~ ~~χ -pod~~ ~~pod~~ method (top) and the MLE fit (bottom) versus χ computed from Chameleon. Note that the MLE method underestimates χ at larger magnitudes. Right: Histograms of the log of ratios for different ranges of ϵ .

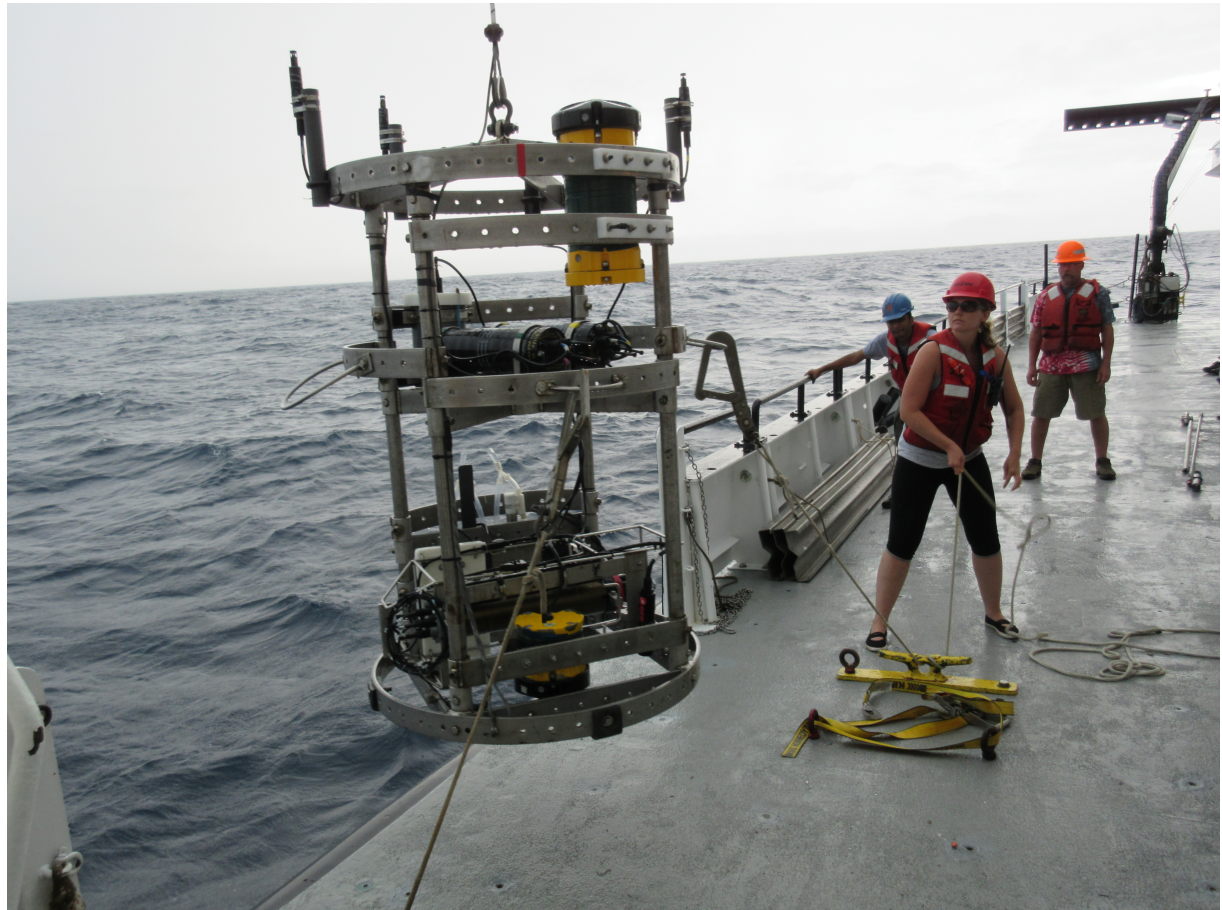
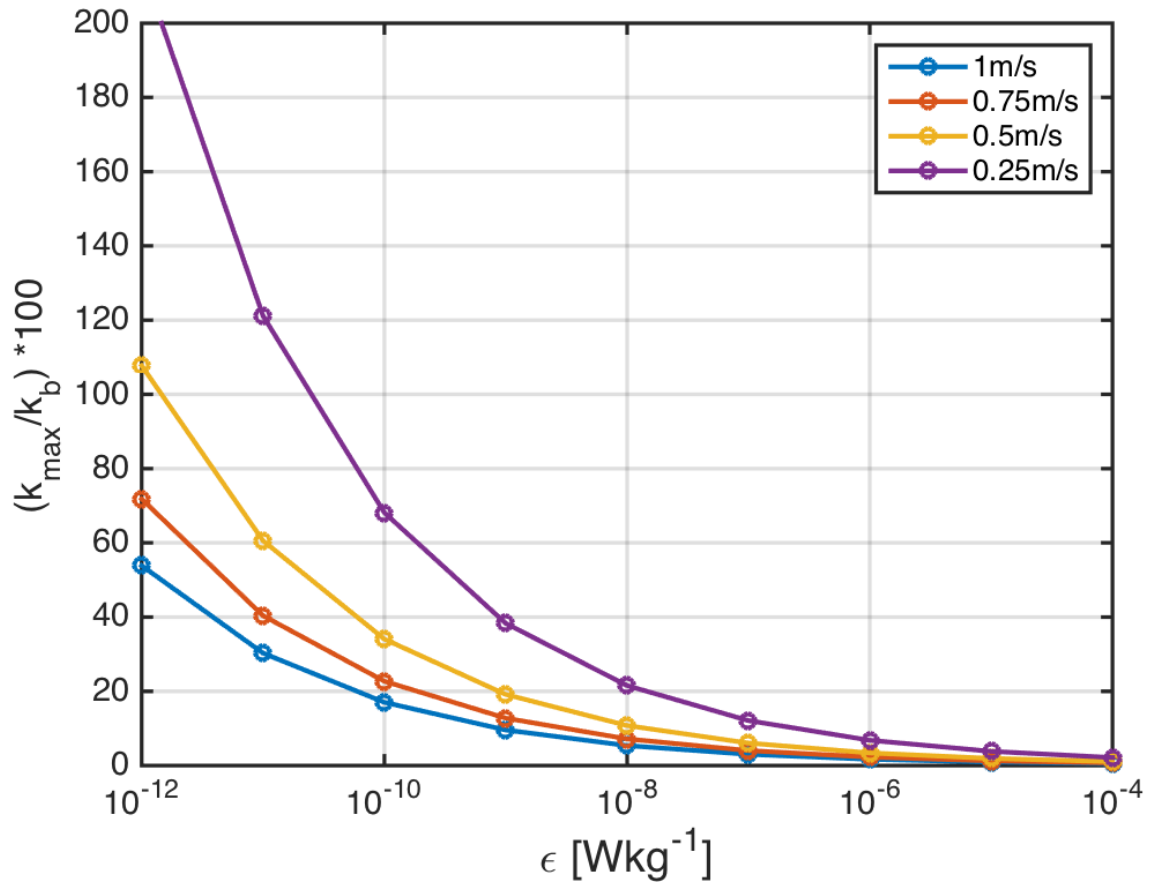
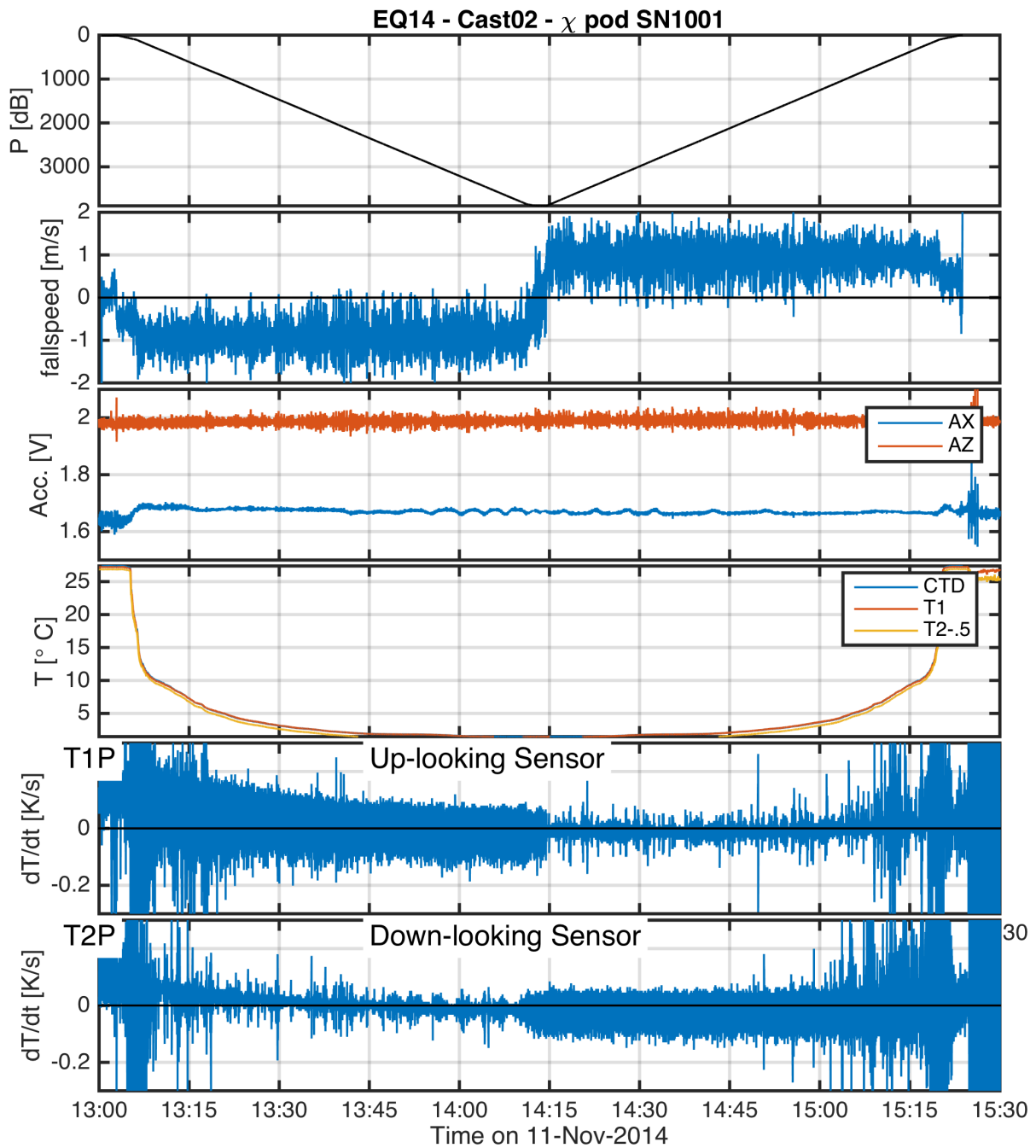


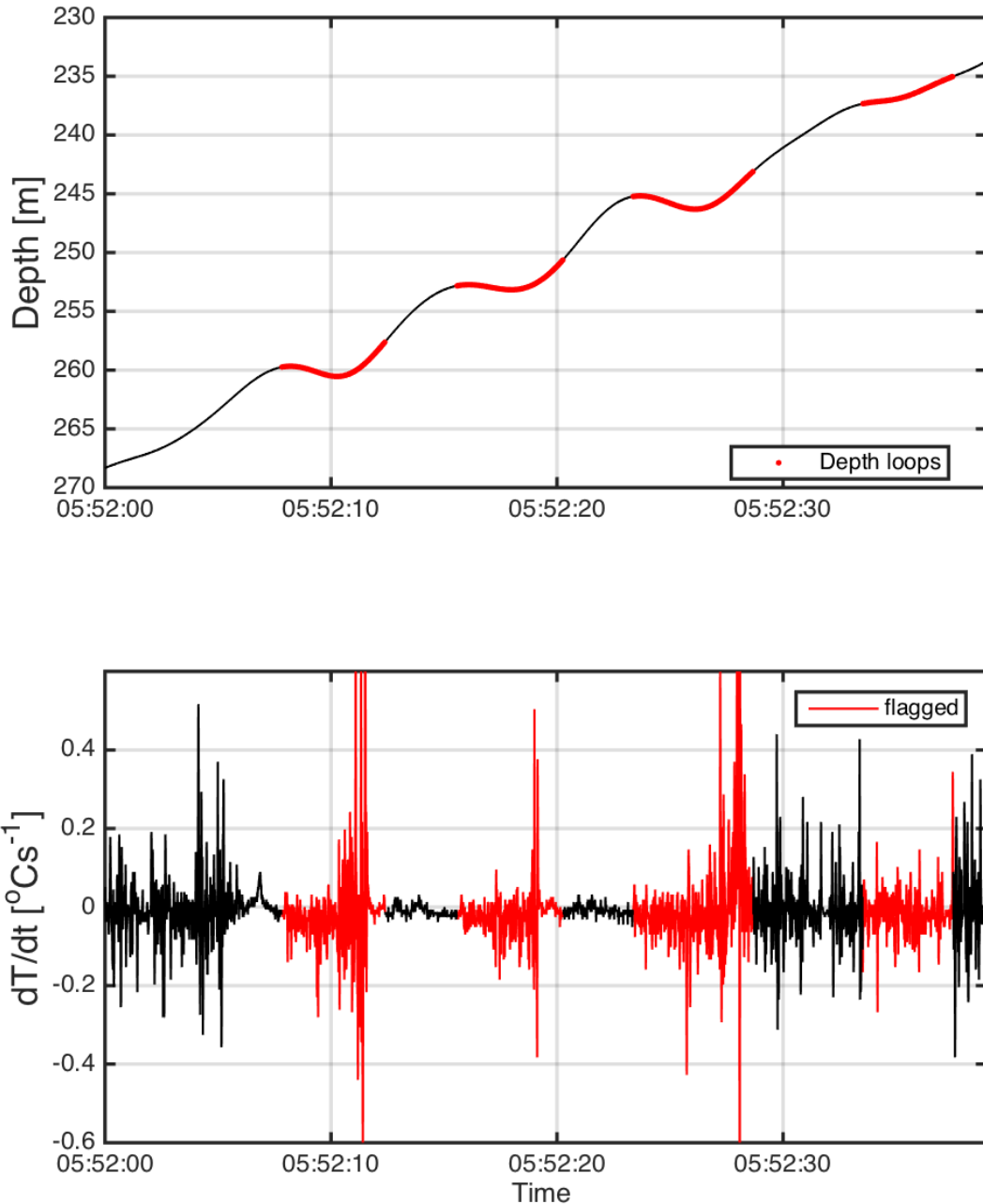
FIG. 1. Photo of CTD rosette during EQ14 with χ -**ped**s-pods attached.



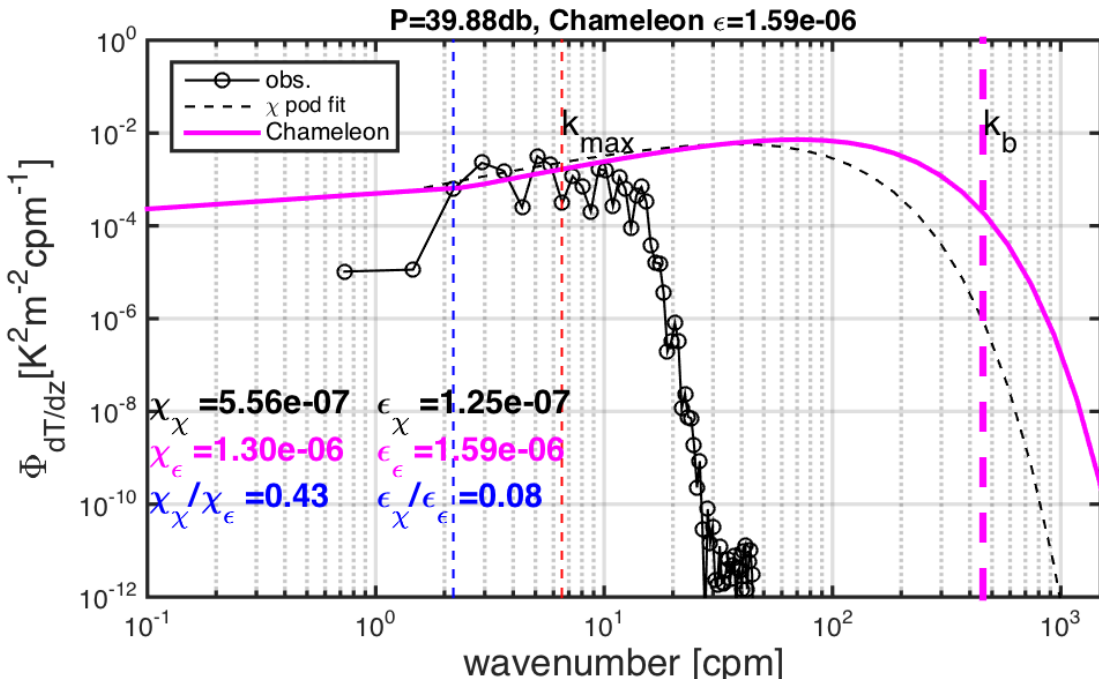
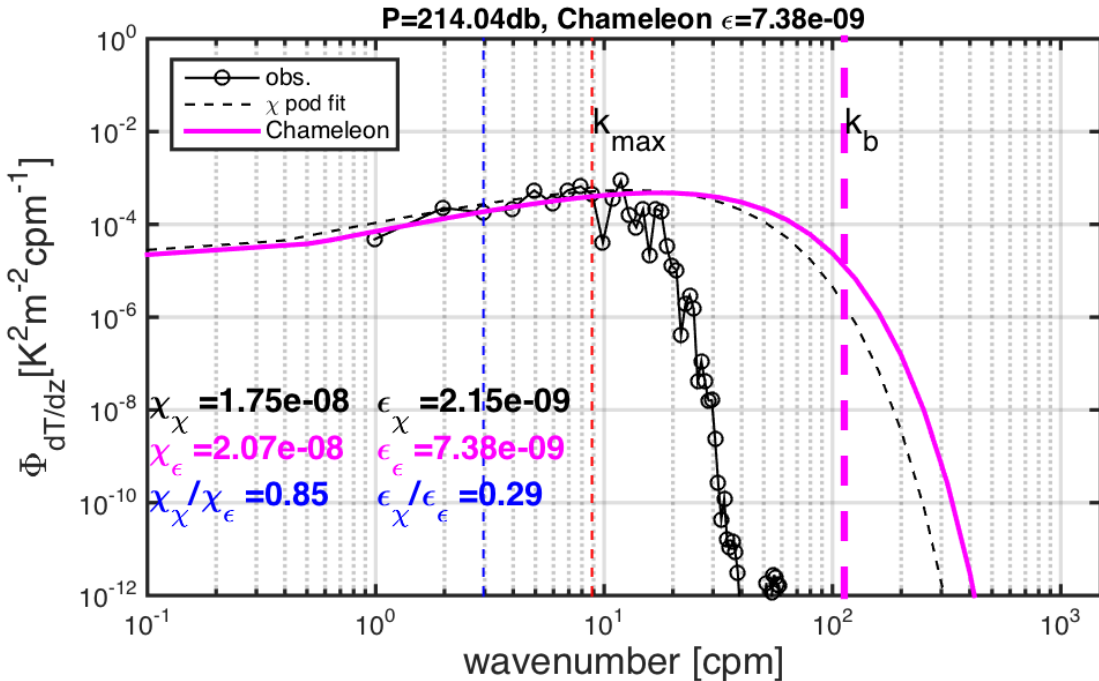
444 FIG. 2. Ratio of the maximum observed wavenumber $k_{\max} = f_{\max}/u$ to the Bachelor wavenumber k_b for
 445 different values of ϵ , assuming a $f_{\max} = 7Hz$. Each line is for a different flowspeed.



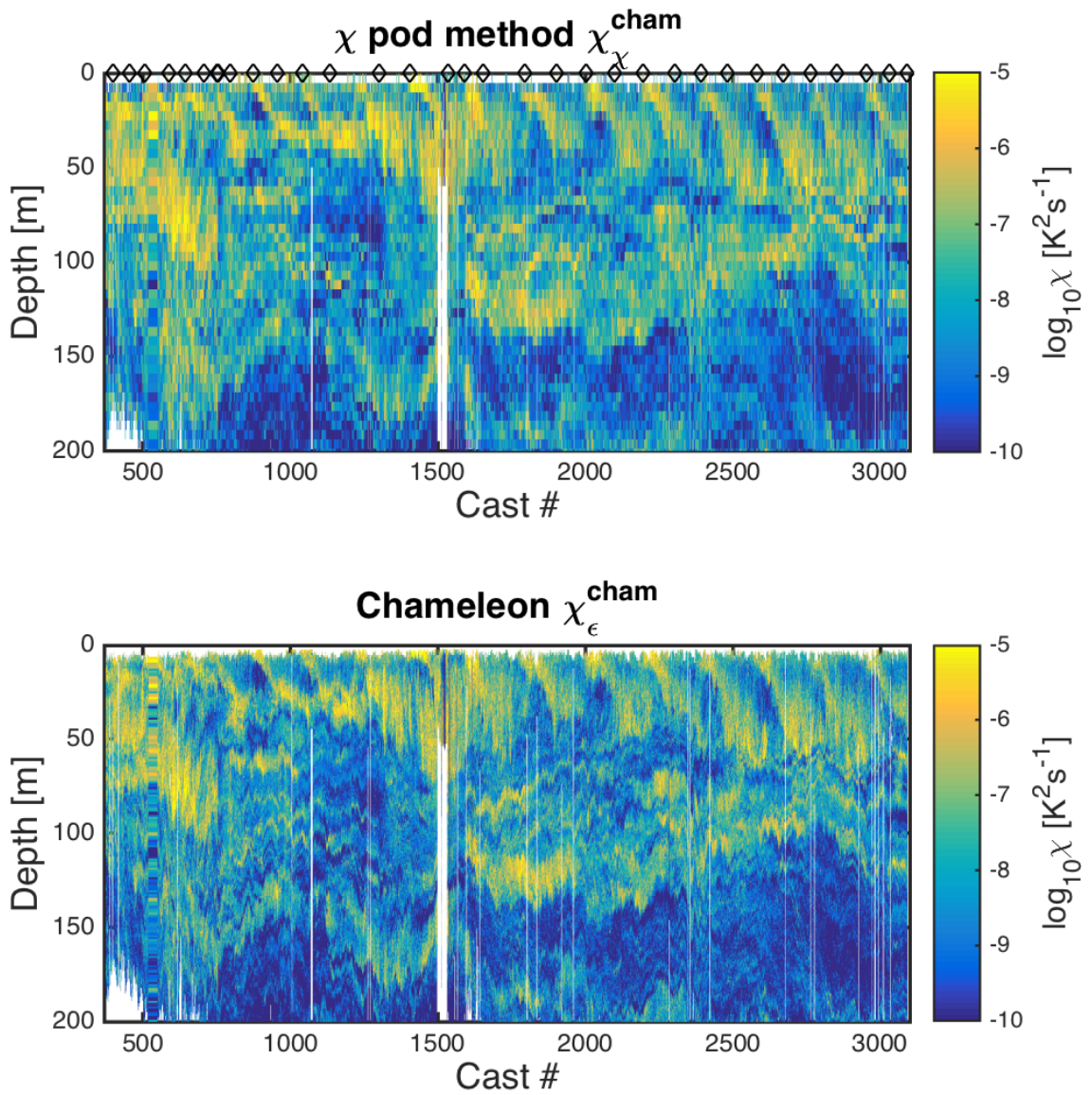
446 FIG. 3. Example timeseries from one CTD cast during EQ14. a) CTD pressure. b) Fallspeed of CTD (dp/dt)
 447 .c) Vertical and horizontal accelerations measured by χ -pod. d) Temperature from CTD and (calibrated)
 448 χ -pod sensors. T2 is offset slightly for visualization. e) Temperature derivative dT/dt measured by the
 449 upward-looking χ -pod sensor T1. f) Temperature derivative dT/dt measured by the downward-looking
 450 χ -pod sensor T2.



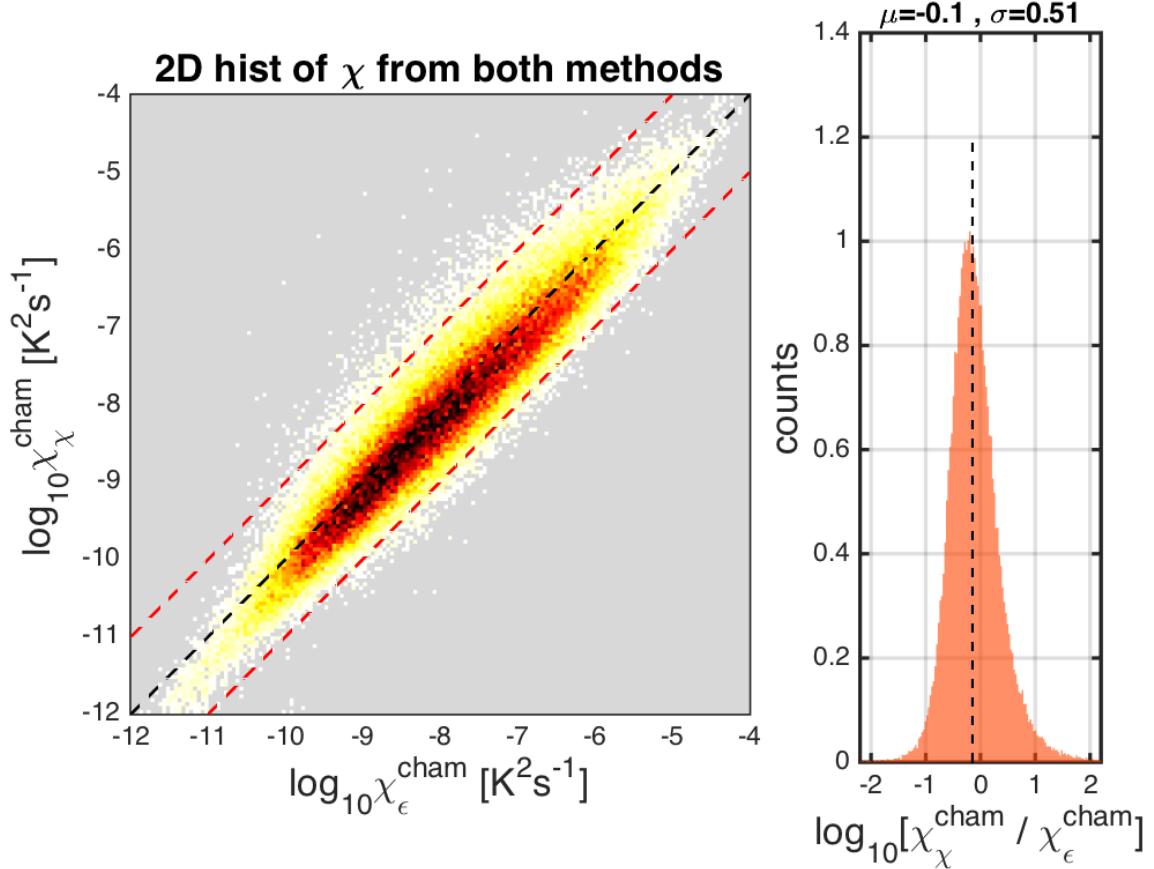
451 FIG. 4. Portion of a CTD cast showing depth vs time (top) during an upcast, with data flagged as loops in red.
 452 Lower panel shows corresponding xpod timeseries of dT/dt for that time with discarded loop data in red. Note
 453 that variance tends to be larger during depth loops due to entrained water and CTD-induced turbulence.



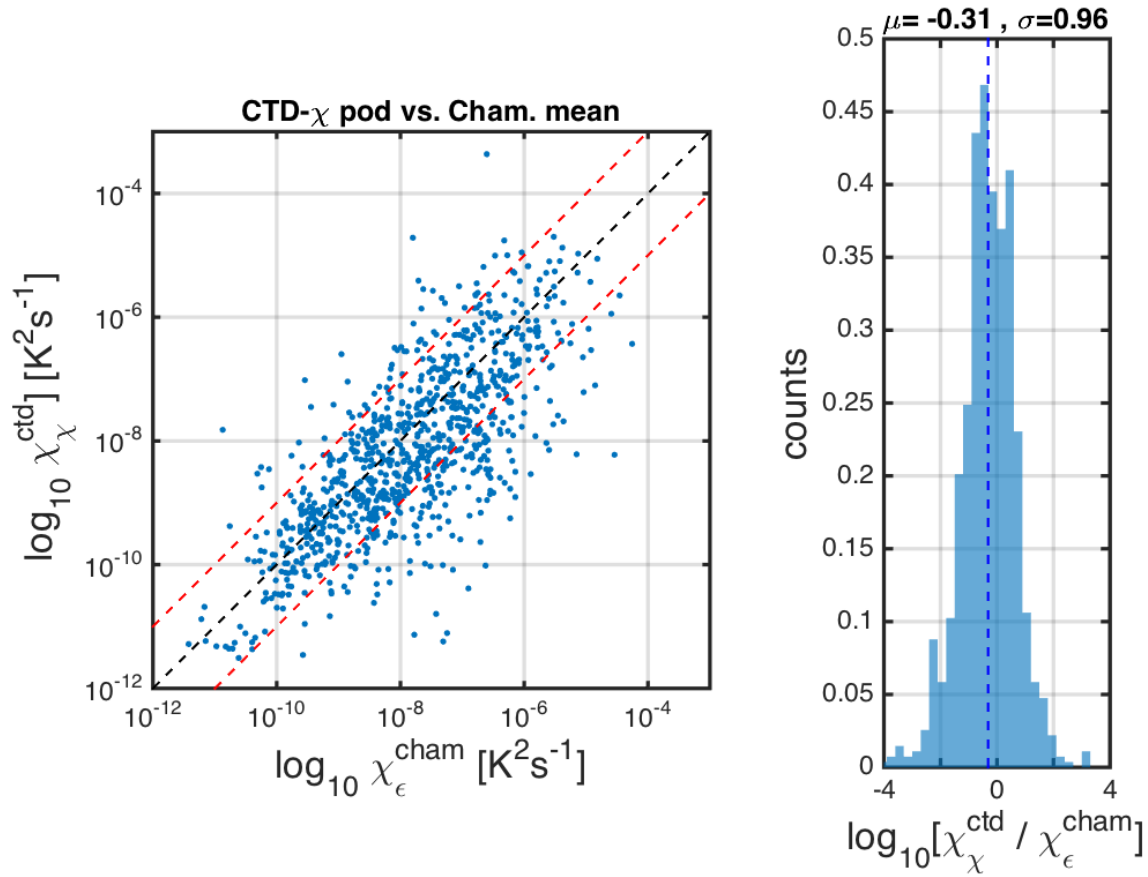
454 FIG. 5. Example Two example temperature gradient spectra from an EQ14 Chameleon profile, for high
 455 (top) and low (bottom) values of ϵ . Solid black line with circles show the observed temperature-gradient
 456 spectra from the thermistor on Chameleon. Dashed black line shows the fitted theoretical Kraichnan spectra for
 457 estimated by applying the χ pod estimates method to the thermistor data only. Magenta line is Kraichnan spectra
 458 for Chameleon χ and ϵ measured at the same depth, using the shear probe data as well. Vertical dashed blue(red)
 459 lines indicate the minimum (maximum) wavenumber used in the χ pod calculation. The Bachelor wavenumber



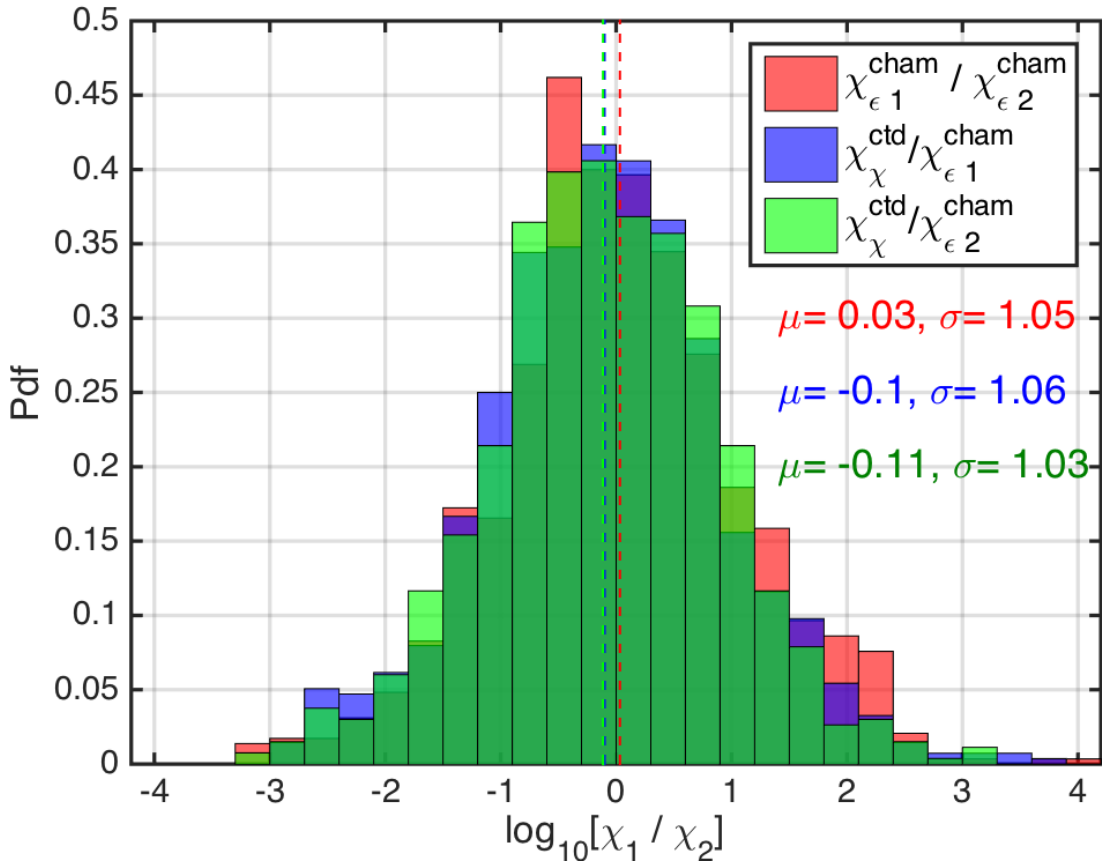
461 FIG. 6. Depth-time plots of $\log_{10}\chi$ from both methods for EQ14 data. Top: χ pod method using only FP07
462 data from Chameleon. Black diamonds indicate casts used for comparison with CTD- χ pod profiles. Bottom:
463 Chameleon measurements using FP07 and shear probe data.



464 FIG. 7. Left: 2D histogram of $\log_{10}(\chi)$ from Chameleon (x-axis) and χ_{pod} method (y-axes). Val-
 465 ues from each profile were averaged in the same 5m depth bins. Right: Normalized histogram of
 466 $\log_{10}[\chi_{\chi}/\chi_{\epsilon}] \log_{10}[\chi_{\chi}^{\text{cham}}/\chi_{\epsilon}^{\text{cham}}]$. Vertical dashed line indicates the mean of the the distribution.



⁴⁶⁷ FIG. 8. Left: Scatter plot of χ from CTD- χ pod profiles versus the mean of bracketing Chameleon profiles.
⁴⁶⁸ Black dashed line shows 1:1, red are $\pm 10 X$. Right: Normalized histogram of the log of ratios.



469 FIG. 9. Histogram of \log_{10} of the ratio of χ for nearby casts. The first set is for the before ($\text{eham1} \chi_{\epsilon 1}^{\text{cham}}$) and af-
 470 ter ($\text{eham2} \chi_{\epsilon 2}^{\text{cham}}$) Chameleon profiles. ~~the~~ The 2nd is CTD- χ pod profiles (χ_{χ}^{ctd}) versus the before($\text{eham1} \chi_{\epsilon 1}^{\text{cham}}$)
 471 profiles. The last is CTD- χ pod profiles (χ_{χ}^{ctd}) versus the after($\text{eham2} \chi_{\epsilon 2}^{\text{cham}}$) profiles. Dashed lines show the
 472 medians of each set. Note that bias is small/zero, and the variability (spread) between CTD/cham is similar to
 473 the natural variability between cham profiles.

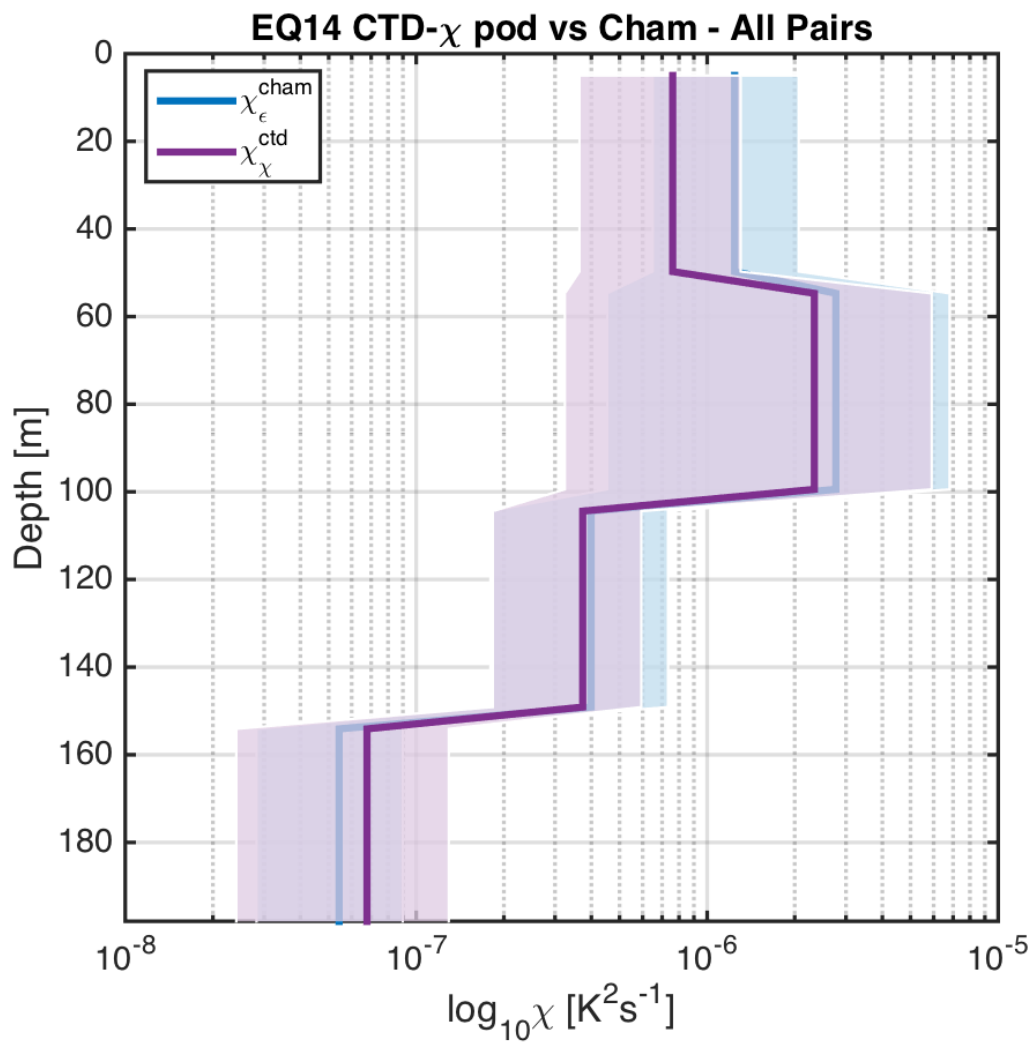
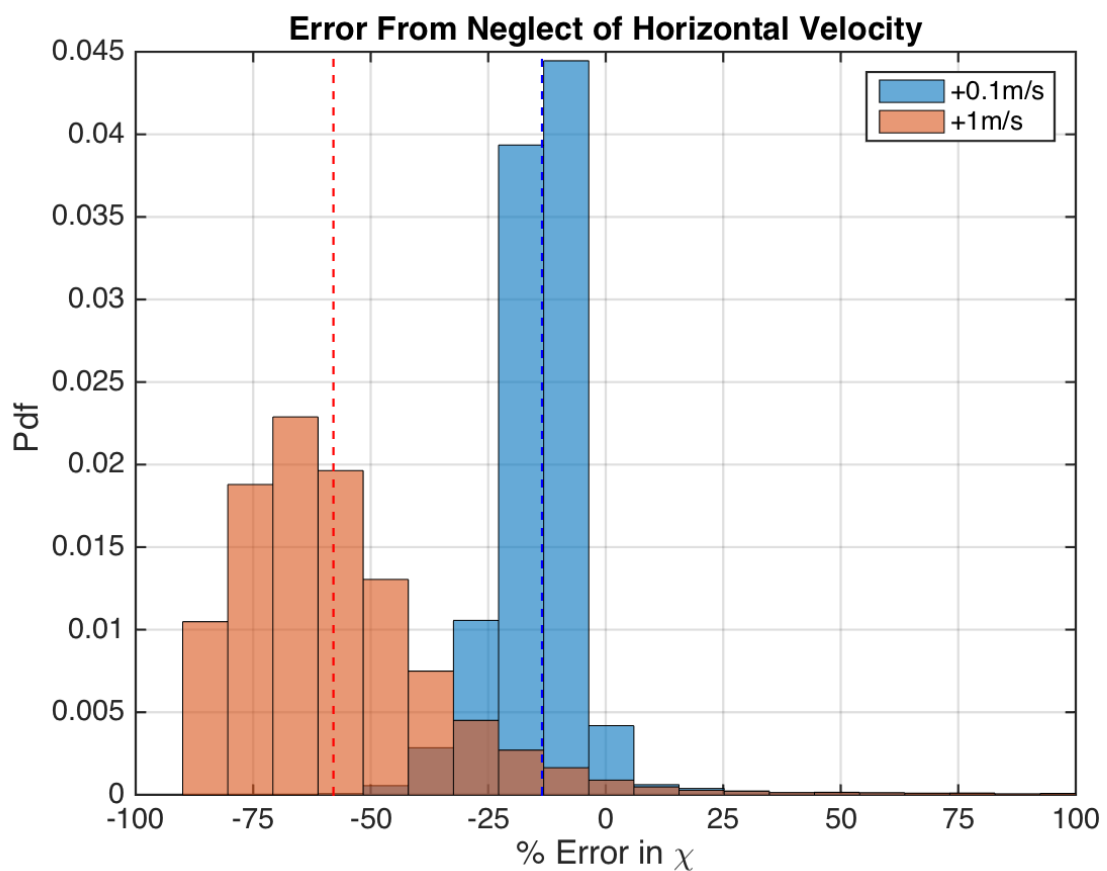
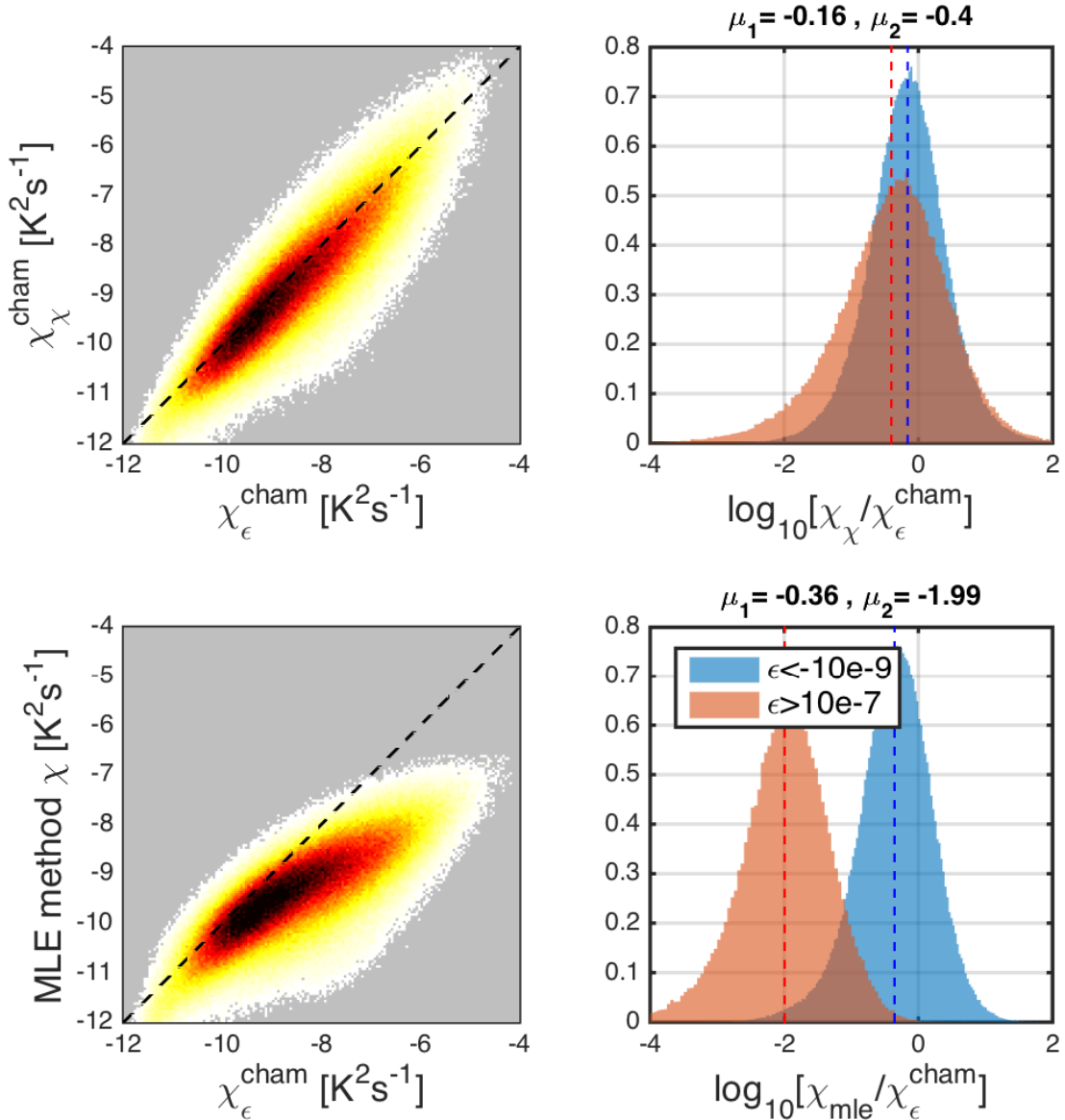


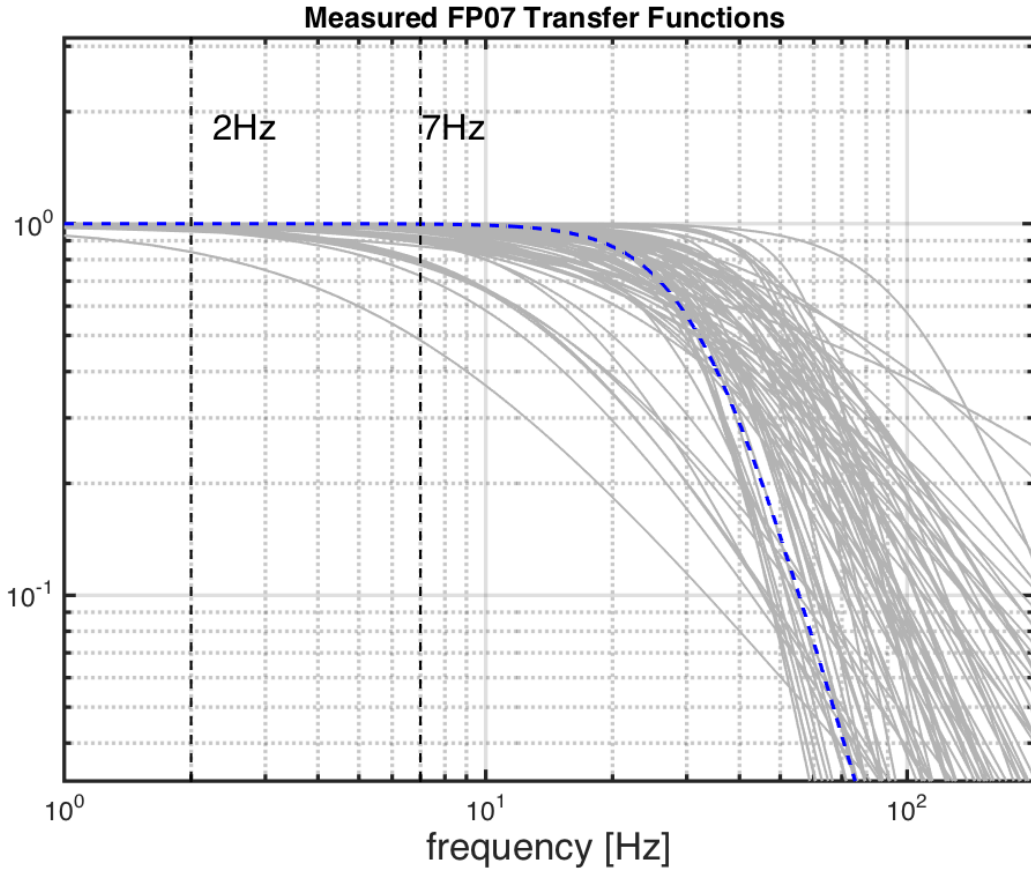
FIG. 10. Time mean of χ for all CTD- χ pod - Chameleon cast pairs, with 95% bootstrap confidence intervals.



474 FIG. 11. Histogram of % error for χ computed with constant added to fallspeed, in order to examine sensitivity
 475 to fallspeed. Vertical lines indicate the mean of each distribution.



476 FIG. 12. Left: 2D histograms of χ computed using the [iterative](#) [iterative](#) [\$\chi\$ -pod](#) [pod](#) method (top) and the
 477 MLE fit (bottom) versus χ computed from Chameleon. Note that the MLE method underestimates χ at larger
 478 magnitudes. Right: Histograms of the log of ratios for different ranges of ϵ .



479 FIG. 13. Measured FP07 thermistor transfer functions from historical database. Vertical dashed lines show
 480 the frequency range used in χ pod method. Dashed blue line is a generic transfer function found to best match
 481 measured functions, and is used when response functions are no longer measured.